Computation of Hypersonic Viscous Flow over a Body with Mass Transfer and/or Spin

M.D. Kim* and C.H. Lewis†
Virginia Polytechnic Institute and State University, Blacksburg, Virginia

Computational results of hypersonic laminar viscous flow over blunt-nosed bodies with mass transfer and/or spin are presented. An implicit-iterative numerical scheme at each marching step is used to solve the parabolized Navier-Stokes equations. The code takes into account the mass-transfer and spin effects in the boundary conditions at the body surface and the periodic effect in the boundary condition around the body. To facilitate convergence, the v-momentum equation has been used rather than the continuity equation to provide the pressure at the body boundary. The coupled effects of mass transfer and spin on the Magnus force and surface measurable quantities were substantial.

Nomenclature

c_p = constant pressure specific heat
CFS = streamwise skin-friction coefficient, $2\tau_x^*/(\rho_\infty U_\infty^2)$
CFW = cross flow skin-friction coefficient, $2\tau_\phi^*/(\rho_\infty U_\infty^2)$
C_A = axial force coefficient
C_N = normal force coefficient
C_Y = Magnus force coefficient
C_m = pitching moment coefficient about blunt nose-tip
C_n = Magnus moment coefficient about blunt nose-tip
$F_{\tau_x} = \sin^2\theta_c \int_0^x \int_0^{2\pi} x\sin\phi\,\tau_x(x,\phi)\,d\phi\,dx$
$F_{p_w} = \tfrac{1}{2}\sin 2\theta_c \int_0^x \int_0^{2\pi} x\sin\phi\, p_w(x,\phi)\,d\phi\,dx$
$F_{\tau_\phi} = \sin\theta_c \int_0^x \int_0^{2\pi} x\cos\phi\,\tau_\phi(x,\phi)\,d\phi\,dx$
FY = total Magnus side force, $F_{\tau_x} + F_{p_w} + F_{\tau_\phi}$
H = total enthalpy, H^*/U_∞^2
h = static enthalpy, $h^*/(C_p^* T_\infty)$
L = reference length, equivalent cone slantwise length
M = freestream Mach number
$\dot{m}$ = mass-transfer rate at wall, $\rho_w^* v_w^*/\rho_\infty U_\infty$
p = nondimensional pressure, $p^*/(\rho_\infty U_\infty^2)$
p_w = wall pressure, $p_w^*/\rho_\infty U_\infty^2$
Pr = Prandtl number
q = heat-transfer rate, $q^*/(\rho_\infty U_\infty^3)$
r = local body radius, r^*/L
R_n = dimensional body nose radius of curvature
Re_∞/ft = freestream unit Reynolds number
$STINF$ = Stanton number, $q^*/[\rho_\infty U_\infty (H_0^* - H_w^*)]$
s = surface distance coordinate measured along the body from nose tip, s^*/R_n
T = temperature, T^*/T_∞
T_0 = freestream stagnation temperature
T_{ref} = reference temperature, $(\gamma-1)M^2 T_\infty$ or U_∞^2/C_p^*
T_w = wall temperature, T_w^*/T_∞
U_∞ = dimensional freestream velocity
u = velocity in the x direction, u^*/U_∞
v = velocity in the y direction, v^*/U_∞
w = velocity in the ϕ direction, w^*/U_∞
x = coordinate along the body surface with constant ϕ, x^*/L
y = coordinate normal to the surface, y^*/L
YSH = bow-shock standoff distance divided by R_n
$Z_{\text{c.p.}}$ = center of pressure from blunt nosetip in percentage of the blunt body axial length
α = angle of attack, deg
γ = ratio of specific heats
η = transformed normal coordinate, y/ξ
ϵ = perturbation parameter, $\epsilon^2 = \mu^*(T_{\text{ref}})/(\rho_\infty U_\infty R_n)$
θ_c = cone half-angle, deg
μ = coefficient of viscosity, μ^*/μ_∞
ξ = bow-shock standoff distance divided by L
ρ = density, ρ^*/ρ_∞
τ_x = primary flow wall shear stress, $\tau_x^*/(\rho_\infty U_\infty^2)$
τ_ϕ = crossflow wall shear stress, $\tau_\phi^*/(\rho_\infty U_\infty^2)$
ϕ = cricumferential coordinate
Ω = angular velocity, rpm

Superscript

* = dimensional quantity

Subscripts

w = wall value
0 = stagnation condition
∞ = freestream condition (dimensional quantity)

Introduction

IN recent years the analysis of hypersonic viscous flows past re-entry vehicles with mass transfer and/or spin has been a problem of considerable interest in ballistics because of its relevance in slowly spinning planetry entry. Previously, a numerical method (VSL3D)[1] based on a viscous shock-layer approach was applied to the computation of heat- and mass-transfer effects on three-dimensional viscous shock-layer flows by Murray and Lewis.[2] The VSL3D method was found to give accurate predictions even at very high altitude, because the code takes into account wall- and shock-slip effects. Another numerical analysis for the mass-transfer effect using the viscous shock-layer theory was given by Whitehead and Davis.[3] The VSL3D method has a restriction on the angle of attack for the entire solution around the body. In other words, since the numerical scheme used is parabolic in the circumferential direction, it cannot treat the cross flow separated region. In the above studies, spin effects on the flowfield were not treated.

Presented as Paper 81-1044 at the AIAA 16th Thermophysics Conference, Palo Alto, Calif., June 23-25 1981; submitted Aug. 24, 1981; revision received April 15, 1982.

*Graduate Student, Aerospace and Ocean Engineering Department. Student Member AIAA.
†Professor. Associate Fellow AIAA.

Recently, a numerical approach for the hypersonic viscous flowfield solution was developed by Lubard and Helliwell[4] using the parabolized Navier-Stokes equations (PNS). The PNS method has been applied to the various problems predicting hypersonic viscous flows over bodies at high angles of attack. For instance, Waskiewicz and Lewis[5] applied the method to a variety of freestream conditions and investigated its limit and applicability. They found that the PNS method could produce accurate predictions of the flowfield during reentry up to at least a 38 deg angle of attack. They also discussed the following effects of axial pressure gradient models. For problems involving high Mach and Reynolds numbers, the implicit pressure gradient model provided unique solutions, regardless of the step size, with no noticeable increase in the number of iterations required for convergence. Problems involving large adverse streamwise pressure gradients due to high angle of attack, large mass transfer, or small Mach and Reynolds numbers can cause difficulties in convergence for the implicit pressure-gradient model. In such cases, an explicit or zero pressure-gradient model was needed, and the accuracy of the solution was dependent on the streamwise step size. In their work, the VSL3D code was satisfactory for the preparation of an initial plane data which were used to start the PNS solution. Later, Gogineni and Lewis[6] reduced the computing times required for an entire solution by combining the VSL3D and PNS methods, and also by using a fast implicit-iterative technique known as the pseudo elimination method. The PNS method has been further developed by Helliwell et al.[7,8] by introducing a more general body-generator coordinate system, thus extending the applicability to more complex bodies. A streamline coordinate system also has been incorporated into the PNS method by Kim et al.[9] in an effort to extend the capability to treat extremely high angles of attack.

Spin effects on the hypesonic viscous flowfields past conical bodies have been computed and analyzed by Agarwal and Rakich.[10] The PNS code by Lubard and Helliwell[4] was modified to include the periodic condition for the flow profiles in the windward plane of a spinning body. They also introduced a new criterion for defining cross flow separation behind spinning bodies, which generalizes the Moore-Rott-Sears criterion for two-dimensional unsteady separation. The onset of separation in the flowfield is characterized by the condition $\partial w/\partial y=0$ at $w=0$, where w is the circumferential component of velocity and y the coordinate normal to the body. Detail analyses were made by Agarwal and Rakich concerning the effects of angle of attack, freestream Reynolds number, nose bluntness, and/or spin rate on the Magnus force components. Coning motion was also considered by Agarwal and Rakich[11] using a further modified PNS method. Another study of the spin effects for cones or ogive-cylinder-boattailed bodies has been reported by Sturek and Schiff,[12] where the results were obtained using another PNS approach. None of the foregoing investigations considered the coupled effects of mass transfer and spin.

In the present study, computational results and discussion are presented for the parametric effects of mass transfer and/or spin together with reasonable computing times consumed for each test case. The original PNS code used the continuity equation to obtain the wall pressure at the body boundary in the case of mass transfer. Theoretically this method appears quite reasonable, because it can provide a finite value for the wall pressure when the normal velocity at wall does not vanish, and, moreover, it is a relatively simple equation. However, by numerical experiment, it has been found that a solution is generally not obtainable by this method in the case of mass transfer. Therefore, in the present work, the v-momentum equation is differenced to provide the wall pressure at the body boundary. In most cases, the flowfield solution has been obtained without convergence problems by the current method.

Analysis

Governing Equations

The governing equations are the laminar, steady, parabolized Navier-Stokes equations derived by Lubard and Helliwell[4] under the assumption that the gradients of the shear stress in the streamwise direction are negligibly small compared with the gradients in the normal and circumferential directions. The resulting equations are parabolic in the streamwise direction and elliptic in the cross flow direction. The governing equations include the continuity, three momentum, and energy equations. The fluid density is given by the equation of state for a perfect gas. Prandtl number and specific heat are assumed constant and Sutherland's viscosity law is used.

In addition to the usual boundary layer order-of-magnitude terms, $d\phi$ is assumed to be $0(\epsilon)$ to include the cross flow separation, and the normal velocity v is taken as 0(1). The flow variables are nondimensionalized by their freestream values. The normal coordinate is normalized by the shock layer thickness to facilitate the computation of the shock location. The complete set of governing equations together with the derivation procedure can be found in Ref. 4.

In the development of these equations, a body-oriented coordinate system is used (Fig. 1), with x taken along the body generator, y normal to the body surface, and ϕ the circumferential coordinate, where $\phi=0$ represents the windward ray. The coordinate system does not rotate with the body.

Boundary Conditions

The following equations are used for the boundary conditions at the body surface with mass transfer and spin.

$$\left(\frac{\partial p}{\partial y}\right)_w = -\frac{1}{r}\frac{\partial(\rho v^2 r)}{\partial y} - \frac{1}{r}\frac{\partial(\rho v w)}{\partial \phi} + \frac{\rho w^2 \cos\theta_c}{r}$$
$$+ \frac{1}{Re}\left(\frac{4}{3}\mu\frac{\partial^2 v}{\partial y^2} + \frac{\partial v}{\partial y}\frac{\partial(4/3\mu)}{\partial y} + \frac{\mu}{r^2}\frac{\partial^2 v}{\partial \phi^2} + \frac{1}{r^2}\frac{\partial v}{\partial \phi}\frac{\partial \mu}{\partial \phi}\right.$$
$$\left. + \frac{1}{r}(\mu+\lambda)\frac{\partial^2 w}{\partial \phi \partial y} + \frac{1}{r}\frac{\partial \mu}{\partial \phi}\frac{\partial w}{\partial y} - \frac{1}{r\xi}(\mu+\lambda)\frac{\partial w}{\partial y}\frac{\partial \xi}{\partial \phi}\right)$$

u = 0
v = specified distribution (mass transfer)
w = specified distribution (spin)
h = specified distribution

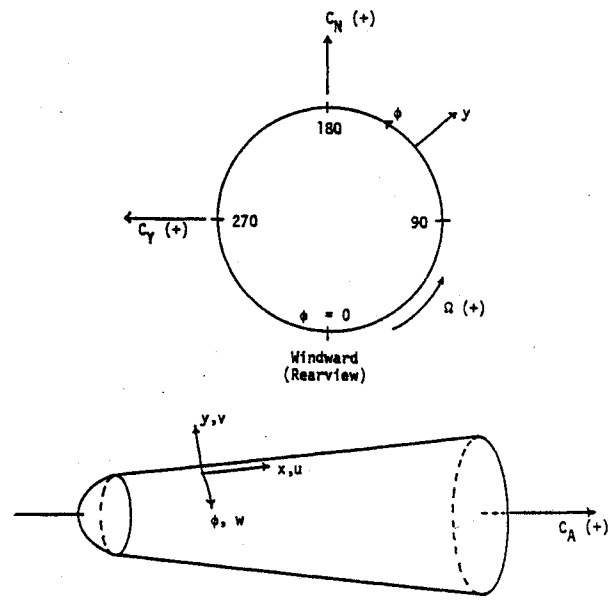

Fig. 1 Body generator coordinate system.

To obtain the wall pressure for the mass-transfer and spin case, the original code utilized the continuity equation; however, numerical experiments showed the method to be inefficient for the convergence of a solution. It has been found that the employment of the v-momentum equation gives a more stable solution. Thus for the present analysis, the v-momentum equation has been taken and differenced using a one-sided differencing scheme to provide the pressure at the body boundary.

In order to obtain the outer boundary conditions, Rankine-Hugoniot jump conditions are utilized at the shock. The components of freestream velocity in the body-oriented coordinate system are:

$$u=\cos\theta_c\cos\alpha-\sin\theta_c\sin\alpha\cos\phi$$

$$v=-\sin\theta_c\cos\alpha-\cos\theta_c\sin\alpha\cos\phi$$

$$w=\sin\phi\sin\alpha$$

From the freestream components and jump conditions, five conservation equations are obtained that can be used to determine the aftershock properties. To uniquely determine the six unknowns—ξ, u, v, w, p, h—at the shock boundary, one more equation is required. Thus the one-sided differencing of the continuity equation provides the sixth equation.

Since the windward and leeward surfaces are not symmetry planes for the spinning cone, a periodic condition for the flow profiles in the windward plane is specified, thus providing the boundary conditions in the ϕ-coordinate direction.

In a rectangular y-ϕ grid, the shock may not fall on a mesh point. To resolve this difficulty, a coordinate transformation, $\eta=y/\xi(x,\phi)$ is made, where $\xi(x,\phi)$ is local shock-layer thickness. Due to the coordinate transformation, the shock-layer thickness ξ appears in all the governing equations, thus requiring one more governing equation, $\partial\xi/\partial\eta=0$, to be differenced.

Initial Conditions

For a numerical flowfield solution that utilizes a marching scheme, preparation of an accurate initial data plane (IDP) is one of the most crucial conditions for a successful start of a solution. By previous investigations,[5,6] the viscous shock-layer method (VSL3D)[1] for blunt bodies was found to be able to generate a satisfactory initial data plane to start the PNS solution. Thus, the entire flow properties, including the shock shape, must be supplied at an initial data plane to get the PNS code started.

Three different methods have been used to generate an initial data plane. The first method is to construct a one-step IDP using the VSL3D method at the sphere-cone juncture. In most cases, the one-step IDP constructed by the VSL3D code was satisfactory to start the PNS solution. The one-step IDP is obtained by an axisymmetric VSL solution and necessary rotations of the solution. In this case, the initial marching step size should be small to start a solution with a gradual increase of the step size downstream of the IDP.

The second method is to prepare a two-step IDP using the VSL3D code at any desired axial station of the body. This method is better than the first one for convergence of the starting solutions, and hence the initial marching step sizes can be taken larger. The third method is to prepare a two-step IDP using the LUB2 code, which is another PNS code described by Agopian et al.[7] for more general bodies. In this method, an axisymmetric VSL solution provides an IDP at the blunt nose for the LUB2 solution, and then the LUB2 code again prepares an IDP at a desired axial station by the necessary three-dimensional calculations. This method is somewhat tedious, but can produce an accurate IDP even when the angle-of-attack is over 30 deg. In the preparation of IDP for the test cases, the spherical nosetips of the bodies had neither spin nor mass transfer; however, including mass transfer over the spherical nose would present no problem, since it has been done in other applications.

Numerical Solution

The equations are solved by implicit differencing in the y, ϕ plane. The x derivatives are approximated by a backward difference, while y and ϕ derivatives use an unequally spaced three-point difference formula, e.g.,

$$\frac{\partial f}{\partial x}=\frac{f_j-f_{j-1}}{\Delta x}$$

and

$$\frac{\partial f}{\partial y}=\alpha_{k-1}f_{k-1}+\alpha_k f_k+\alpha_{k+1}f_{k+1}$$

where the α_i are determined from the Taylor series expansions of f_{k-1} and f_{k+1} around the kth location; hence, they are functions of the step size between the grid points.

The PNS equations and the perturbation equations during the iterations can be written in the matrix form

$$\boldsymbol{F}(\boldsymbol{U})=0$$

$$\boldsymbol{\Delta}^n=\boldsymbol{U}^{n+1}-\boldsymbol{U}^n$$

where $\boldsymbol{F}$ denotes the governing equations for the unknowns $\boldsymbol{U}$, and $\boldsymbol{\Delta}^n$ is the column matrix of perturbation properties at nth iteration.

After differencing, the equations are linearized by the Newton-Raphson method. Thus, all the nonlinear terms of perturbation properties are dropped. This procedure results in an equation of the form

$$\underline{\underline{M}}(\boldsymbol{U}^n)\boldsymbol{\Delta}^n=-\boldsymbol{F}(\boldsymbol{U}^n)\qquad n=0,1,2,\ldots$$

with $\boldsymbol{U}^0$ an initial guess to the solution of the governing equations, and $\underline{\underline{M}}$ the Jacobian of $\boldsymbol{F}$. Because of the size of the system, instead of solving the above equation directly, the Gauss-Seidel iteration method is used. In the ϕ direction, an implicit-iterative scheme[8] is used, but after convergence, the solution obtained is a fully implicit one. After convergence, another step in the marching direction is taken and the whole procedure is repeated.

Convergence problems often occur when the marching solution encounters a strongly separated region due to cross flow. To eliminate the problem, either zero or an explicit pressure gradient model may be used. Smaller marching step sizes and/or pressure smoothing in the y coordinate direction also can help the convergence. When the angle of attack is very high, more careful selection of grid sizes and preparation of more accurate initial plane data are required in order to start a solution.

Mass transfer and spin add more disturbances in the viscous flowfield, thus deteriorating the convergence of the solution. A large mass-transfer distribution along the body can cause an axial flow separation at some downstream station which causes the marching solution to fail. To reduce the marching step size problem in a solution, the marching step sizes are controlled internally by the code considering the number of iterations taken for the solution at the previous step.

Results and Discussion

For the present study, a body-generator coordinate system is used with x along the body, y normal to the body, ϕ around the body, and the coordinate system not rotational with the body. Figure 1 shows the coordinate system and the sign conventions for the aerodynamic coefficients. Since this sign convention is not a universal one, it is recommended to be used only for the interpretation of the directions of the forces and moments reported herein.

Table 1 Test case freestream conditions and body geometries

Case	s U_∞, fps	M T_∞, °R	Re_∞, 1/ft α, deg	R_n, ft θ_c, deg	T_w, °R T_w/T_0	ϵ	Ω, rpm	$\dot{m}$, max
1a	30.06 2341	5 91.247	621,000 2	0.027917 7	460 0.84	0.0218	2000	0.00250 dist.[a]
1b	30.06 2341	5 91.247	621,000 2	0.027917 7	460 0.84	0.0218	2000	0.00125 const.[b]
2	30.06 7223	18 64.80	544,740 15	0.027917 7	540 0.1266	0.0545	8000	0.00125 const

[a] Asymmetric distribution around body and constant along body.
[b] Constant around and along body.

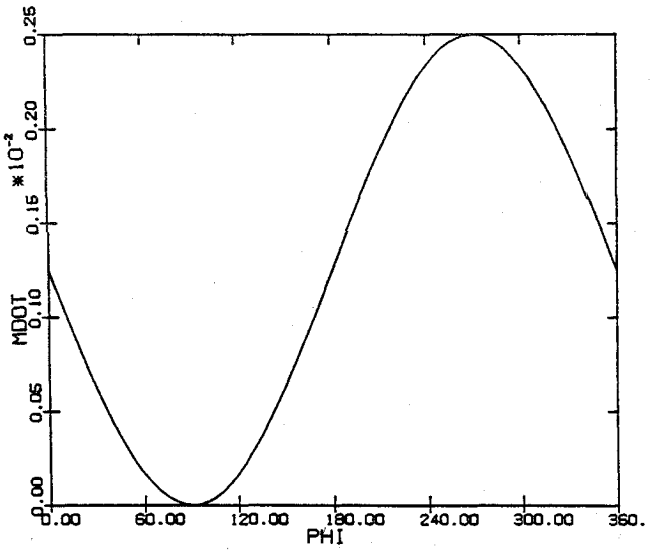

Fig. 2 Asymmetric mass-transfer distribution around the body (case 1a).

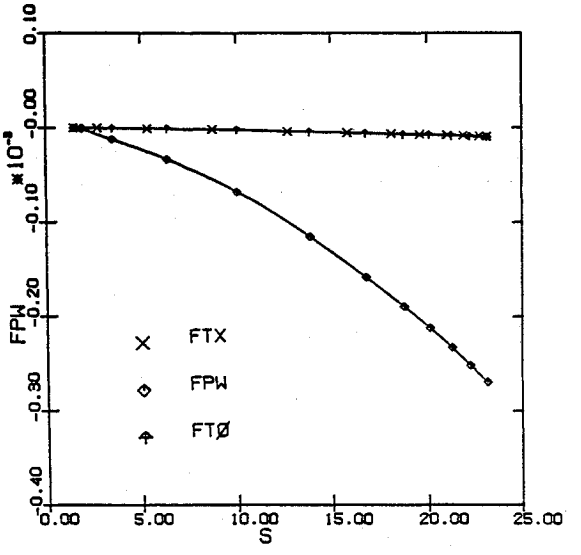

Fig. 4 Magnus force components along the body with mass transfer and spin (case 1a).

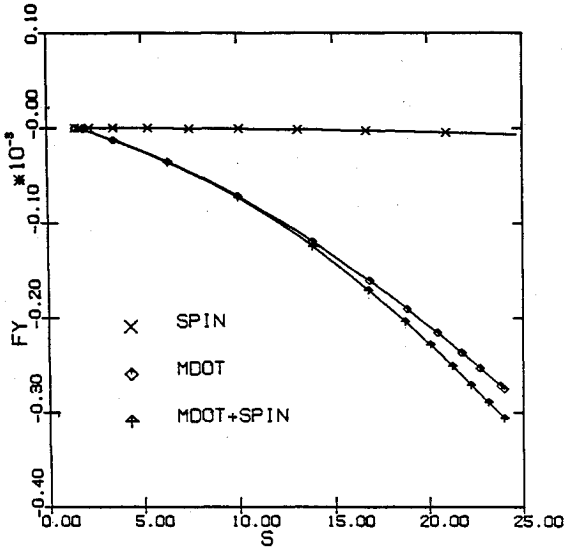

Fig. 3 Effects of asymmetric mass transfer and spin on the Magnus force along the body (case 1a).

The initial plane data for the test cases have been obtained using a perfect gas viscous shock-layer approach (VSL) at the sphere-cone tangent point, and all the flow properties together with forces and moments are transferred to the PNS solution. To start the PNS solution, an initial marching step size of less than one-tenth of the nose radius has been used, and it was increased internally in the code, considering the number of iterations taken and the maximum permissible marching step size for a meaningful solution. In the present calculations, 101 grid points in the normal direction and 19 planes around the body are used for all cases.

In the case of high angle of attack with large mass transfer and spin, relatively large perturbations can occur in the viscous flowfield. These perturbations have an adverse effect on the convergence of a solution. For this reason, in the present computations, the zero pressure-gradient model in the marching direction was used to improve the convergence. The effect of the three different kinds of axial pressure-gradient models has been discussed in detail by Waskiewicz and Lewis.[5]

To investigate the effect of mass transfer and/or spin on the viscous flow past a sphere-cone geometry, two sets of freestream conditions have been chosen and parametric computations have been made. Case 1 considers a freestream condition of $M=5$, $\alpha=2$ and $Re_\infty/\text{ft}=6.21\times10^5$. Case 2 considers a freestream condition of $M=18$, $\alpha=15$ and $Re_\infty/\text{ft}=5.45\times10^5$. The body geometry is a spherically blunted 7-deg half-angle cone, 0.817 ft long. For both cases, a parametric comparison is presented to study the effect of spin, mass transfer, and the coupled effect of both. For case 1, the effect of the asymmetric mass-transfer distribution around the body as well as constant mass-transfer distribution will be analyzed in detail. Spin rates considered are 2000 and 8000 rpm. Case 1a has a sinusoidal mass-transfer distribution around the body, and the maximum value of mass-transfer rate is 0.0025. Cases 1b and 2 have a mass-transfer rate of

0.00125, which is constant along and around the body. Details of the freestream conditions are given in Table 1.

For case 1, the flowfield solution over the body with mass transfer could not be obtained up to the body end. For case 1a with mass transfer only, the solution was obtained up to $s=24.8$, where axial flow separation occurred due to the mass-transfer effect. For case 1a with both mass transfer and spin, the solution was obtained up to $s=23.3$ before axial flow separation occurred.

Figure 2 shows a sinusoidal distribution of mass transfer for case 1a, which is designed to exert a relatively large side force in the minus direction. In Fig. 3, the Magnus force due to the sinusoidal mass-transfer distribution is shown, and it can also be observed that the coupled effect of mass transfer and spin on the Magnus force is remarkable. Figure 4 shows the Magnus force components distribution along the body for case 1a, where it is noted that the Magnus force component due to the wall pressure distribution constitutes the largest part of the total Magnus force, while the components due to the axial and circumferential shear stresses are negligible.

For case 1b, we have constant mass transfer around the body. Hence, in this case, the Magnus force due to mass transfer should be negligible. In Fig. 5, it is noted that the Magnus force due to the coupled effect of the mass transfer and spin is substantial, and the effect is over three times as much as the spin-only effect on the Magnus force.

Figure 6 shows the effect of mass transfer and spin on the Magnus force for case 2 which has relatively large Mach number and high angle of attack. For this case, it is noted that the coupled effect of mass transfer and spin is again remarkable. Therefore, on the basis of the present computational results, it is concluded that this coupled effect should not be neglected in a flight dynamics analysis of a slow-spin re-entry vehicle with mass transfer. Figure 7 shows that the Magnus force component due to the cross flow shear stress is not negligible, and it has a different direction from the F_{p_w} for case 2.

The effect of mass transfer and spin on the wall pressure is shown in Fig. 8, where the spin effect was almost negligible. Hence the differences shown are largely due to mass transfer. It is noted that the mass-transfer effect increases the wall pressure, because the thickening of the viscous layer increases the displacement-induced pressure interaction. In this figure an unstable solution due to axial flow separation can be seen at $s=24$ and $\phi=180$ deg.

Figure 9 shows the effect of mass transfer on axial flow separation for case 1a. In the figure it can be observed that mass transfer retards the axial flow velocity in the boundary layer. The effect becomes larger further downstream and, finally, the axial flow separates at $s=24$, as can be seen in the figure. The PNS method cannot treat the axial flow separated region, hence the solution diverged at this station. In the downstream region before axial flow separation, the numerical solution took a relatively large number of iterations and small marching step sizes. This effect resulted in the relatively large computing time for this case, as can be seen in Table 3.

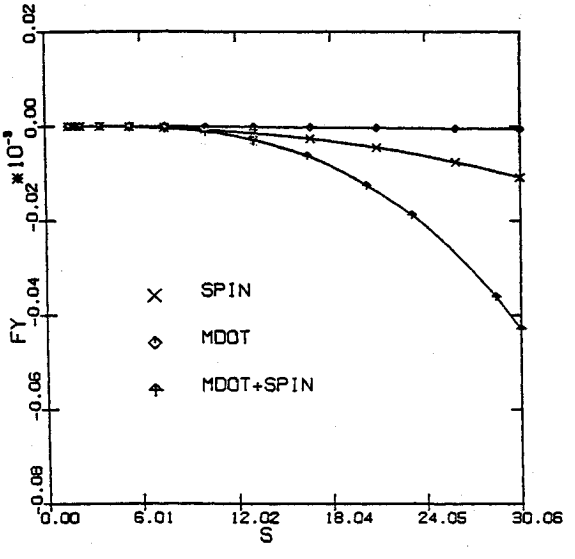

Fig. 5 Effects of constant mass transfer and spin on the Magnus force along the body (case 1b).

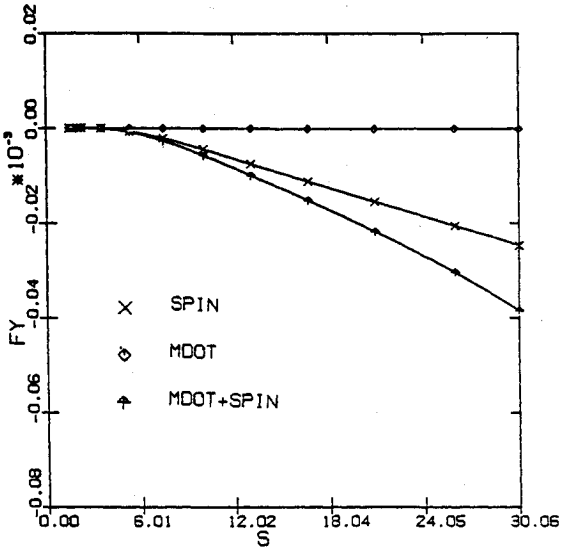

Fig. 6 Effects of constant mass transfer and spin on the Magnus force along the body (case 2).

Table 2 Aerodynamic coefficients for test cases[a]

Case	$\dot{m}$, max	Ω, rpm	C_A	C_N	C_Y	C_m	C_n	$Z_{c.p.}$
1a, basic	0.0	0.0	0.1880	0.0372	−0.0	−0.0214	0.0	0.577
1a, Ω only	0.0	2000	0.1880	0.0372	−0.1850E−3	−0.0214	0.1280E−3	0.577
1a, $\dot{m}$ only	0.00250 dist.	0.0	0.1849	0.0285	−0.8471E−2	−0.0148	0.4902E−2	0.520
1a, $\Omega+\dot{m}$	0.00250	2000	0.1849	0.0284	−0.9392E−2	−0.0147	0.5609E−2	0.517
1b, $\Omega+\dot{m}$	dist. 0.00125	2000	0.1840	0.0307	−0.594E−3	−0.0166	0.4560E−3	0.538
2, basic	0.0	0.0	0.2070	0.4740	−0.0	−0.3075	0.0	0.649
2, Ω only	0.0	8000	0.2070	0.4740	−0.5285E−3	−0.3075	0.3388E−3	0.649
2, $\dot{m}$ only	0.00125 const.	0.0	0.2005	0.4703	−0.0	−0.3050	0.0	0.648
2, $\Omega+\dot{m}$	0.00125 const.	8000	0.2005	0.4703	−0.8246E−3	−0.3050	0.5396E−3	0.648

[a] Cases 1a and 1b: integrated up to $s=23.0$; case 2: integrated up to $s=30.06$.

Table 3 Computing times[a] for test cases

Case	s	s Steps	Grid size of n points	ϕ Planes	Time, min
1a, basic	30.06	45	101	19	37
1a, Ω only	30.06	45	101	19	37
1a, $\dot{m}$ only	24.80	82	101	19	73
1a, $\dot{m}+\Omega$	23.33	70	101	19	65
1b, $\dot{m}+\Omega$	30.06	58	101	19	54
2, basic	30.06	45	101	19	38
2, Ω only	30.06	45	101	19	38
2, $\dot{m}$ only	30.06	45	101	19	40
2, $\dot{m}+\Omega$	30.06	45	101	19	40

[a] CPU time on IBM 3032, H = OPT2 compiler.

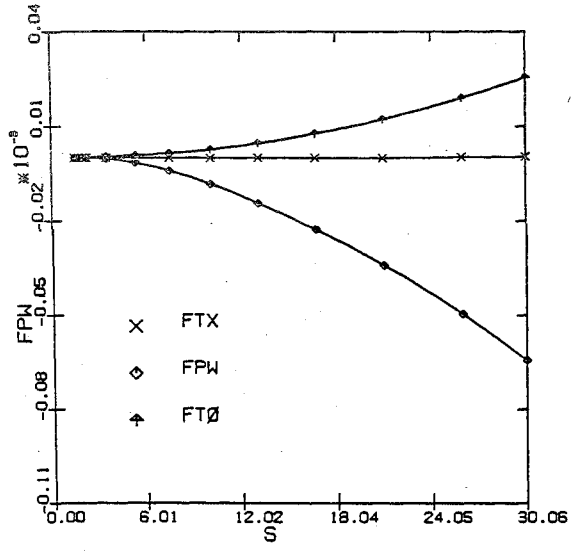

Fig. 7 Magnus force components along the body with mass transfer and spin (case 2).

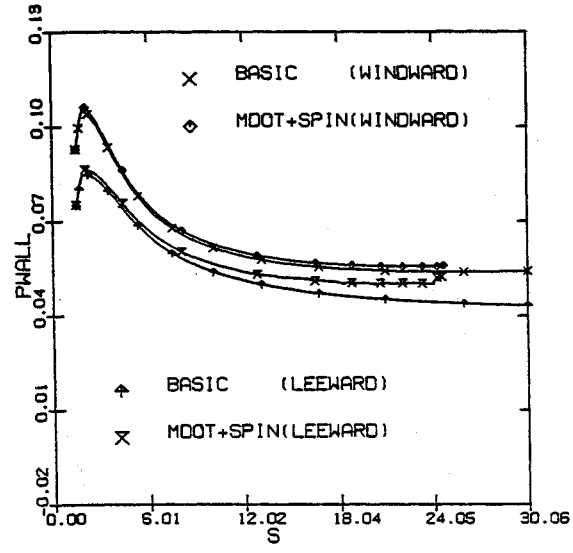

Fig. 8 Effects of mass transfer and spin on the surface pressure along the body (case 1a).

Case 2 had a spin rate of 800 rpm and constant mass-transfer rate of 0.00125. The computational results for this case showed more sizable effects of spin on the wall pressure and other surface properties. Hence, parametric comparisons will be presented for this case. Figure 10 shows the coupled effect as well as the separate effects of mass transfer and/or

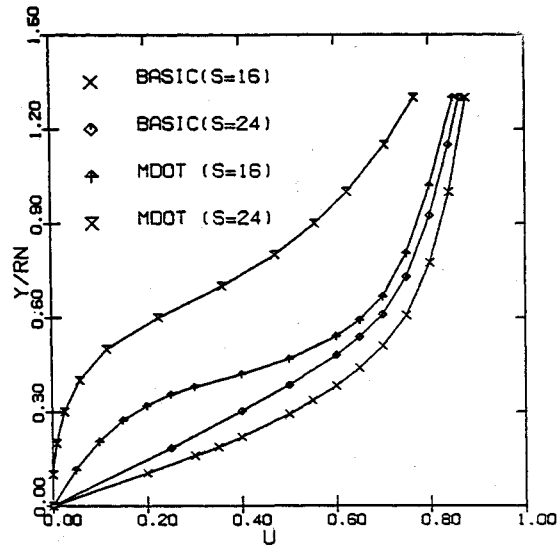

Fig. 9 Effects of mass transfer on the axial flow separation (case 1a).

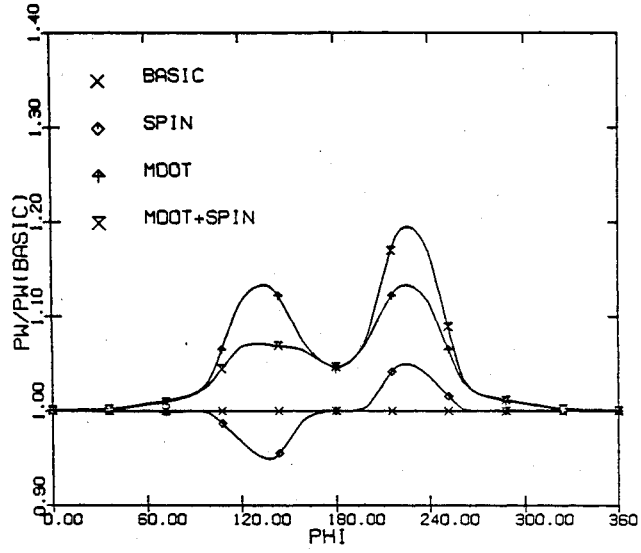

Fig. 10 Effects of mass transfer and/or spin on the surface pressure around the body at $s = 30.06$ (case 2).

spin on the wall pressure. In this figure, the spin effect appears antisymmetric, while the mass-transfer effect is symmetric around the body. The coupled effect is quite clear, and it has a nearly additive characteristic. The spin effect decreases the pressure in $\phi = 0$-180 of the body, and increases the wall pressure in $\phi = 180$-360 of the body, thus producing a negative Magnus force as can be expected. The symmetric mass-transfer itself cannot produce a Magnus force, but it increases the wall pressure symmetrically. Figure 11 shows the effect of mass transfer and spin on the heat transfer in the windward and leeward planes; the effect of mass transfer and/or spin on the streamwise wall shear is shown in Fig. 12.

Table 2 summarizes all the force and moment coefficients obtained from the parametric computations for the two test cases. The effect of the spin on the axial and normal force is found to be negligible, while the effect on the Magnus side force is sizable. An asymmetric mass transfer can also produce a finite amount of side force. From the table, it is also observed that the mass transfer decreases the normal and axial forces. An important fact found in the present work is that mass transfer and spin have a measurable coupled effect on the Magnus side force, which is shown in Table 2 as well as in the figures. However, no experimental data are known to

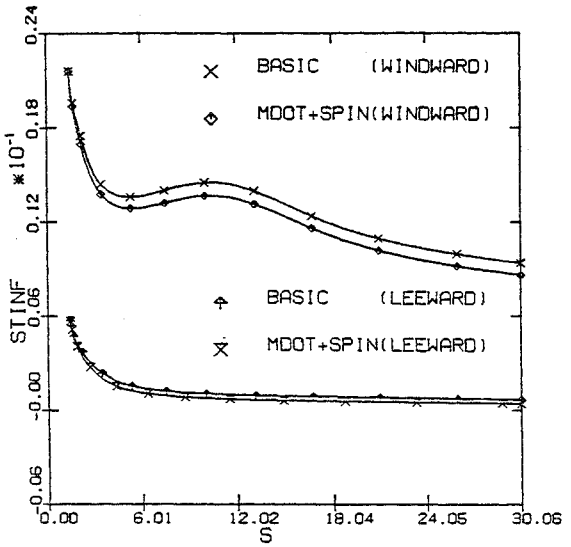

Fig. 11 Effects of mass transfer and spin on the heat transfer along the body (case 2).

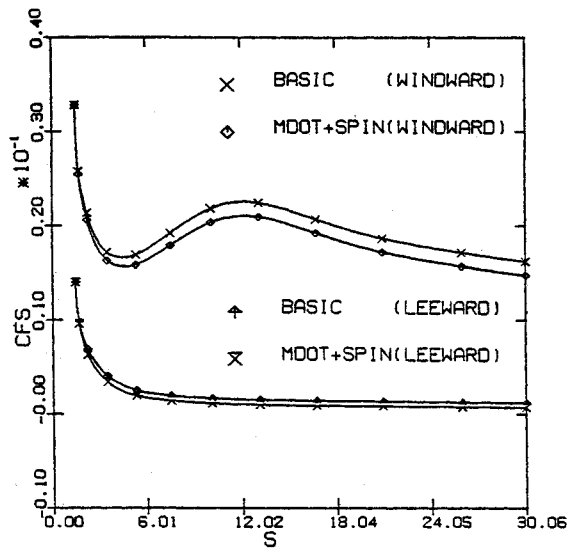

Fig. 12 Effects of mass transfer and spin on the streamwise shear along the body (case 2).

the authors at this time to validate the present results for the coupled effects.

Computing times for these cases are given in Table 3. These times were obtained on an IBM 3032 system. Most cases consumed less than 40 min of CPU time for the entire solution, but the solutions for cases 1a and 1b with mass transfer took relatively longer computing time because of the small step sizes taken before the axial flow separation.

Conclusions

The viscous flowfield over a sphere-cone undergoing mass transfer and/or spin at angle of attack has been calculated using the parabolized Navier-Stokes equations. In the mass-transfer case, the wall pressure is obtained using the v-momentum equation rather than the continuity equation to facilitate the convergence. The main results of the present work can be summarized as follows.

1) The coupled effect of mass transfer and spin on the Magnus force is remarkable, i.e., it is much more than the sum of the two separate effects.

2) Mass transfer has a tendency to reduce axial and normal forces, increase wall pressure, and decrease heat transfer and wall shear stresses.

3) Mass transfer causes earlier axial and cross flow separations.

4) Spinning motion has negligibly small affect on the normal and axial forces, and it produces asymmetric effects on the wall pressure as well as the other surface properties around the body.

5) Spin has a tendency to suppress the appearance of cross flow separation at high angles of attack.

Acknowledgment

This research was partially supported by the Office of Naval Research under Contract N00014-79-C-0328.

References

[1] Murray, A.L. and Lewis, C.H., "Hypersonic Three-Dimensional Viscous Shock-Layer Flows over Blunt Bodies," *AIAA Journal,* Vol. 16, Dec. 1978, pp. 1279-1286.

[2] Murray, A.L. and Lewis, C.H., "Heat and Mass-Transfer Effects on Three-Dimensional Viscous Shock-Layer Flows," AIAA Paper 78-844, May 1978.

[3] Whitehead, R.E. and Davis, R.T., "Numerical Solutions to the Viscous Shock-Layer Blunt Body Problem with Inert Gas Injection," Sandia Laboratories, SC-CR-70-6162, Jan. 1971.

[4] Lubard, S.C. and Helliwell, W.S., "Calculation of the Flow on a Cone at High Angle of Attack," *AIAA Journal,* Vol. 12, July 1974, pp. 965-974.

[5] Waskiewicz, J.D. and Lewis, C.H., "Hypersonic Viscous Flows over Sphere-Cones at High Angles of Attack," AIAA Paper 78-64, Jan. 1978.

[6] Gogineni, P.R. and Lewis, C.H., "Three-Dimensional Viscous Hypersonic Flows over General Bodies," AIAA Paper 80-0029, Jan. 1980.

[7] Agopian, K., Collins, J., Helliwell, W.S., Lubard, S.C., and Swan, J., "NASA Viscous 3-D Flowfield Calculations," R&D Associates, RDA-TR-6100-007, Oct. 1975.

[8] Helliwell, W.S., Dickinson, R.P., and Lubard, S.C., "HYTAC Phase I Report, Viscous Flow over Arbitrary Geometries at High Angle of Attack," Arete Associates Technical Report, AR-79-046-TR, April 24, 1979.

[9] Kim, M.D., Thareja, R.R., and Lewis, C.H., "Three-Dimensional Viscous Flowfield Computations in a Streamline Coordinate System," *AIAA Journal,* Vol. 19, No. 1, Jan.-Feb. 1982, pp. 41-46.

[10] Agarwal R. and Rakich, J.V., "Computation of Hypersonic Laminar Viscous Flow Past Spinning Sharp and Blunt Cones at High Angle of Attack," AIAA Paper 78-65, Jan. 1978.

[11] Agarwal, R. and Rakich, J.V., "Computation of Supersonic Laminar Viscous Flow Past a Pointed Cone at Angle of Attack in Spinning and Coning Motion," AIAA Paper 78-1211, July 1978.

[12] Sturek, W.B. and Schiff, L.B., "Computations of the Magnus Effect for Slender Bodies in Supersonic Flow," AIAA Paper 80-1586, 1980.